

See discussions, stats, and author profiles for this publication at: <https://www.researchgate.net/publication/231646953>

# Meso- and Macroporous Co<sub>3</sub>O<sub>4</sub> Nanorods for Effective VOC Gas Sensors

ARTICLE *in* THE JOURNAL OF PHYSICAL CHEMISTRY C · APRIL 2011

Impact Factor: 4.77 · DOI: 10.1021/jp1116189

---

CITATIONS

75

READS

110

## 2 AUTHORS:



[Nguyen Duc Hoa](#)

Hanoi University of Science and Technology

83 PUBLICATIONS 1,165 CITATIONS

[SEE PROFILE](#)



[Sherif El-Safty](#)

National Institute for Materials Science

168 PUBLICATIONS 3,241 CITATIONS

[SEE PROFILE](#)

# Meso- and Macroporous $\text{Co}_3\text{O}_4$ Nanorods for Effective VOC Gas Sensors

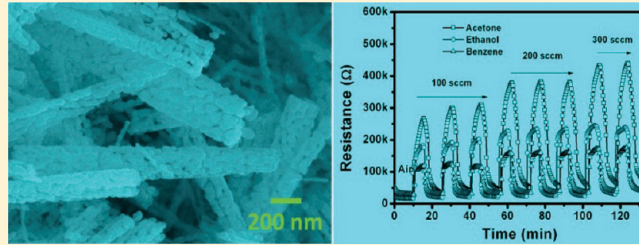
Hoa Nguyen<sup>†</sup> and Sherif A. El-Safty\*,<sup>†,‡</sup>

<sup>†</sup>National Institute for Materials Science (NIMS), 1-2-1 Sengen, Tsukuba-shi, Ibaraki-ken 305-0047, Japan

<sup>‡</sup>Graduate School for Advanced Science and Engineering, Waseda University, 3-4-1 Okubo, Shinjuku-ku, Tokyo 169-8555, Japan

Supporting Information

**ABSTRACT:** The synthesis of crystalline nanorod metal oxides with porous structure is an important issue in gas sensor technology, which aims to increase their sensitivity and stability. In addition, the development of a facile method to synthesize large yields of nanorods is a key factor in reducing the cost of products in thick film gas sensor technology. Large yields of crystalline meso-/macroporous  $\text{Co}_3\text{O}_4$  nanorods are fabricated using facile hydrothermal method from  $\text{CoCl}_2$  and urea precursors, without using any surfactants or template-directing agents. The gas-sensing properties of synthesized nanorods are tested to volatile organic compounds (VOCs) such as benzene, acetone, and ethanol. Results reveal that crystalline meso- and macroporous  $\text{Co}_3\text{O}_4$  nanorods have the highest sensitivity to acetone with a fast response and a recovery time of one minute. Moreover, the sensing properties of crystalline meso-/macroporous  $\text{Co}_3\text{O}_4$  nanorods depend strongly on carrier (reference) gases, whereas preadsorbed oxygen plays an important role in the sensing mechanism of  $\text{Co}_3\text{O}_4$ -based nanorod sensors for VOCs.



## 1. INTRODUCTION

Environmental pollution is a critical problem all over the world because it leads to the depletion of the ozone layer, global warming, and climate change.<sup>1</sup> Moreover, it also affects our health as it causes cancers, birth defects, and mental retardation.<sup>1c</sup> Among the contaminants in air, volatile organic compounds (VOCs), such as benzene, acetone, and toluene, are the most common and dangerous because they not only pollute the environment but also directly affect human's health. For instance, benzene is a known organic compound that causes serious environmental health concerns because of its toxicity and carcinogenic properties, even at low concentrations.<sup>2</sup> Breathing low levels of benzene can cause drowsiness, dizziness, rapid heart rate, headaches, tremors, confusion, and unconsciousness. Unlike benzene, acetone is believed to exhibit only a slight toxicity with normal use, but its hazard lies in its extreme flammability. The materials safety data sheet of acetone announces that at a temperature higher than flash point ( $-20^\circ\text{C}$ ), air mixtures of between 2.5% and 12.8% acetone by volume may explode or cause a flash fire. Despite their toxicity and hazard, VOCs are still used in industries as intermediates to produce other chemicals and as solvents in research laboratories. The probability of over exposure to such toxic agents are very high; therefore, the development of gas sensors for early detection of flammable and/or toxic gases is necessary.

To date, there has been a great deal of research toward the development of miniaturized gas-sensing devices and the

improvement of sensor performance, particularly for toxic gas detection and for environmental pollution monitoring.<sup>3</sup> Researchers are trying to look for suitable materials and special structures that could be used to develop better gas sensors that have fast response, long-term stability, high sensitivity, and greater selectivity.<sup>4</sup> So far, attempts have been focused on the development of n-type semiconducting metal oxide-based gas sensors, such as  $\text{SnO}_2$ ,  $\text{ZnO}$ ,  $\text{TiO}_2$ ,  $\text{In}_2\text{O}_3$ , and  $\text{WO}_3$ .<sup>5</sup> Few works have dealt with p-type semiconducting metal oxide-based gas sensors.<sup>6</sup> Among the p-type semiconductors,  $\text{Co}_3\text{O}_4$ , with a direct band gap of about 2 eV, is one of the most interesting prospects because it has several potential applications such as in pigments, electrochemistry, magnetism, catalysis, batteries, and especially gas sensors.<sup>7</sup> For instance, Zhang et al. reported on the use of  $\text{Co}_3\text{O}_4$  loaded on  $\text{SnO}_2$  for ethanol and acetone detection, in which the sensor response was about seven and five times as large as that of the pure  $\text{SnO}_2$ , respectively.<sup>8</sup> Patil et al. reported that  $\text{Co}_3\text{O}_4$  nanorods showed high sensitivity and fast response to  $\text{CO}$ .<sup>9</sup>

On the other hand, according to the sensing mechanisms of gas sensors, the adsorption/desorption processes mainly take place on the surface of the sensing layer and determine the response of the sensors. The sensitivity of gas sensors depends on

**Received:** December 7, 2010

**Revised:** March 8, 2011

**Published:** April 12, 2011

the size, shape, and specific surface area of the sensing material.<sup>10</sup> A porous structure with a higher specific surface area of sensing layers produces better gas sensor performance and shows fast response and recovery time, high sensitivity, and low limited detection of gaseous concentration.<sup>11</sup> To date, hydrothermal and solvothermal methods have been developed for the synthesis of different nano/microstructured  $\text{Co}_3\text{O}_4$ , such as nanocubes, nanosheets, nanobelts, nanogranulars, nanorods, and nanospheres.<sup>12</sup> However, recent reports indicate that hydrothermal or solvothermal synthesis of  $\text{Co}_3\text{O}_4$  require the use of various substances, including cobalt source, and surfactants and/or structure-directing agents, making its fabrication difficult. The development of a facile method to synthesize nanostructured materials with the ability to control their pores, shape, and size still remains a challenge.<sup>13</sup> Furthermore, the hydrothermal synthesis of porous  $\text{Co}_3\text{O}_4$  nanorods for benzene, and acetone gas sensor application is rarely reported. There has not been any report about the effects of carrier and reference gases on the sensing properties of porous  $\text{Co}_3\text{O}_4$  nanorods.

In this paper, we introduce the use of high crystalline meso- and macroporous  $\text{Co}_3\text{O}_4$  nanorods for effective acetone, benzene, and ethanol gas sensors application. Crystalline meso-/macroporous  $\text{Co}_3\text{O}_4$  nanorods are reproducibly synthesized via a facile hydrothermal method, using cobalt chloride and urea as precursors. This simple synthesis method allows the obtainment of large yield of products. It has the ability to control the morphologies and meets the growing demand for mass production of nanorods required in thick film gas sensor technology. The gas-sensing properties of synthesized nanorods are investigated to volatile organic compounds (VOCs) such as benzene, acetone, and ethanol at different temperatures. The meso-/macroporous  $\text{Co}_3\text{O}_4$  nanorods have been found to be effective in the detection of acetone. In this study, the effects of carrier and reference gases on the sensing properties of  $\text{Co}_3\text{O}_4$  are also investigated to understand the sensing mechanisms of sensors. Resistance change (increase or decrease) is dependent on the carrier gases, in which preadsorbed oxygen plays an important role in the response of sensors.

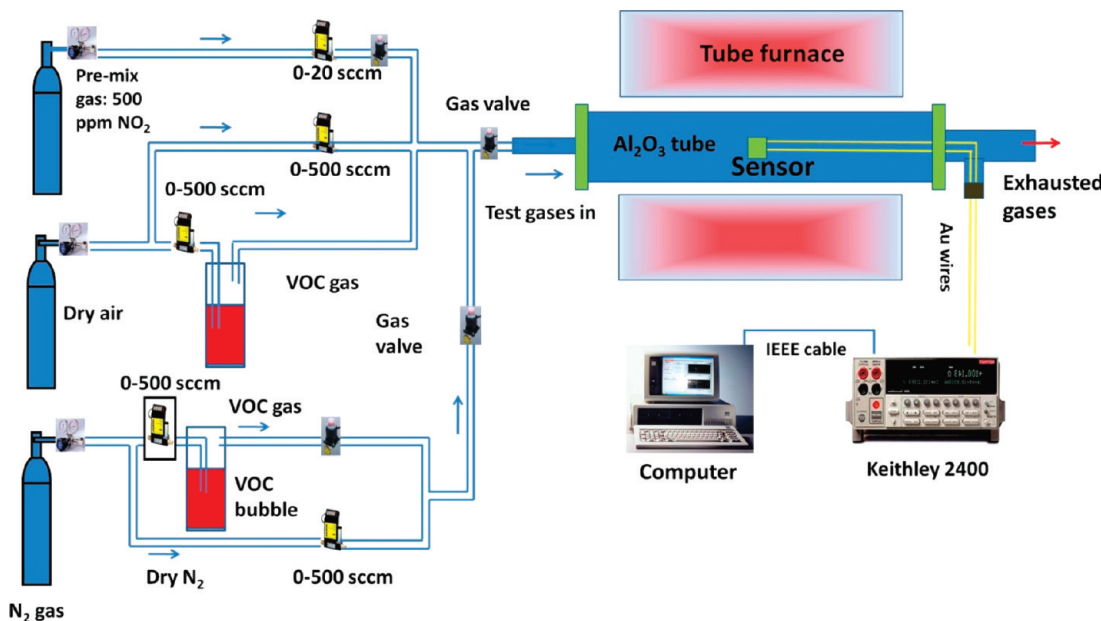
## 2. EXPERIMENTAL SECTION

**2.1. Synthesis of Meso- and Macroporous  $\text{Co}_3\text{O}_4$  Nanorods.** The hydrothermal synthesis of meso-/macroporous  $\text{Co}_3\text{O}_4$  nanorods using cobalt chloride and urea as starting precursors, but without using any further surfactants or template-directing agents, was adapted from ref 14 with some modifications. In our preparation method, the concentration of precursor solution ( $\text{CoCl}_2$ ) and the ratio of urea/cobalt salts were increased to obtain larger yield of product (Figure S1, Supporting Information). To produce crystalline nanorods, the calcination temperature and time (at 500 °C for 8 h) were also applied. In a typical synthesis, a 50 mL transparent solution of  $\text{CoCl}_2$  (0.2 M) and  $\text{CH}_4\text{N}_2\text{O}$  (0.4 M) was poured into a Teflon-lined autoclave of 100 mL in volume. The autoclave is sealed and placed in an oven for hydrothermal processing. The hydrothermal is performed at 180 °C for 16 h and then allowed to cool at room temperature. After the hydrothermal process, the pink precipitate is collected by centrifuging the solution at 4000 rpm and rinsed several times with distilled water and ethanol before being dried at 50 °C. Finally, the meso- and macroporous  $\text{Co}_3\text{O}_4$  nanorods are formed into black powders by calcining the pink precipitate in a tube furnace at 500 °C for 8 h. The product yield was estimated

by comparing both the weights of the obtained nanorods and the starting precursor. Up to ~94.1% of solid product could be obtained by using our synthesis conditions. In addition, by scaling up the volume of autoclave and using high concentration of precursors, a large amount of nanorods is obtained easily, as evidenced from the FESEM image (Figure S2, Supporting Information). The FESEM image provided evidence of the formation of porous  $\text{Co}_3\text{O}_4$  nanorods with high  $\text{CoCl}_2$  concentration of 0.25 and starting volume solution of 95 mL. The large yield reproducibly synthesized nanostructured products is very important because most of the latest commercial gas sensor devices are produced using the thick film technique, where the use of large amounts of sensing materials is necessary.

**2.2. Characterization.** The morphologies of as-synthesized and calcined products were investigated using field emission scanning electron microscopy (FE-SEM, JEOL model 6500). The as-synthesized and calcined powders were attached to a specimen stub using a double-sided carbon tape. Next, a 10 nm Pt film was coated using an ion-sputter (Hitachi E-1030) to prevent the accumulation of electrostatic charge on the surface of the samples during measurement. The elemental analyses were investigated by energy-dispersive X-ray spectroscopy using an X-ray microanalyzer (SEM-EDS), which was embedded in the JEOL model 6500. The FE-SEM and SEM-EDS were operated with an acceleration voltage of 15 kV. High-resolution transmission electron microscopy (HRTEM), electron diffraction (ED), scanning transmission electron microscope (STEM), and dispersive X-ray analysis for elemental mapping (STEM-EDS) were characterized using a JEOL, JEM model 2100F microscope. The HRTEM was operated by applying an acceleration voltage of 200 kV to obtain a lattice resolution of 0.1 nm and the spherical aberration of 1.0 mm. The STEM and STEM-EDS were operated at a camera length of 80 and a spot size of 1 nm. The HRTEM and STEM images were recorded using a CCD camera. In the HRTEM, the STEM, and the STEM-EDS characterization, the nanorods were dispersed in an ethanol solution using an ultrasonic cleaner and then dropped on a carbon grid. Before insetting in the HRTEM column, the grid was vacuum-dried for 20 min. The crystal structure of  $\text{Co}_3\text{O}_4$  was studied by X-ray diffraction (XRD, Bruker HI-Star) using  $\text{CuK}\alpha$ -X-radiation with a wave-number of  $\lambda = 1.54178 \text{ \AA}$ . Specific surface area and pore size were determined using  $\text{N}_2$  adsorption–desorption isotherms at 77 K with a BELSORP analyzer (JP. BELCo. Ltd.).

**2.3. Gas-Sensing Characterizations.** The gas sensors were fabricated using the thick film technique. Powders of meso- and macroporous  $\text{Co}_3\text{O}_4$  nanorods were mixed with methyl cellulose organic binders,  $\alpha$ -terpineol, and distilled water in an agate mortar to form a slurry. The slurry was then pasted on a substrate supported electrodes for electrical and gas-sensing measurements. The organic binders were removed by annealing at 400 °C for 1 h. From the cross sectional FESEM image (Figure S3, Supporting Information), the average final film thickness of sensor sample was about 30  $\mu\text{m}$ . The electrical and gas-sensing properties were measured in a tube furnace, as shown in Scheme 1. For electrical measurements, golden wires were placed in contact with electrodes using silver paste. Dry air or high-purity nitrogen (5N) was used as carrier (reference) gas. The test gases were generated by bubbling carrier gases through the bubbler solution (benzene, acetone, and ethanol). Concentrations of VOCs were calculated using the equation  $C(\text{ppm}) = 10^6 \times (P_{\text{sf}}/P(f+F))$ , where f and F are the flow rates (in sccm) of the bubbling air (or  $\text{N}_2$ ) saturated with VOC and the air (or  $\text{N}_2$ )

Scheme 1. Schematic Diagram of Gases Sensing Measurement System<sup>a</sup>

<sup>a</sup>The tested and referenced gases are mixed using series of mass flow controllers. The electrical current and resistance of sensors are automatically measured using a Keithley model 2400 controlled by PC computer via IEEE cable and Labview program.

as dilution gas, respectively; P is the total pressure (760 mmHg); and  $P_S$  is the saturated partial vapor pressure obtained using the Antoine equation.<sup>15</sup> The gas-sensing properties were measured in a dynamic condition, in which the carrier gas and the tested gas continuously flowed through the sensing chamber, with a total flow rate of 500 sccm during the measurements. Prior to the test, the sensors were preheated at 400 °C for 30 min to increase the stability of the sensors. A desired concentration of the test gases (VOCs) was introduced into the sensing chamber for 5 min and then switched to dry air (or N<sub>2</sub>) for recovery. The current and resistance were automatically recorded using a digital source-meter (Keithley model 2400) and controlled using a laptop PC via KUSB-488A interface using a Labview program (see Scheme 1). The sensor response S was defined as  $S = 100 \times (R - R_0)/R_0$  (in the case of measurement in air) and  $S = 100 \times (R_0 - R)/R$  (in the case of measurement in N<sub>2</sub>). R and R<sub>0</sub> are a form of sensor resistance in the presence of test gas and carrier gas (air or N<sub>2</sub>), respectively.

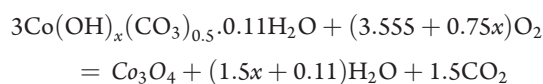
### 3. RESULTS AND DISCUSSION

**3.1. Characteristics of Meso-/Macroporous Co<sub>3</sub>O<sub>4</sub> Nanorods.** The meso- and macroporous Co<sub>3</sub>O<sub>4</sub> nanorods were basically prepared by applying the parent method, as reported by Wang et al.<sup>14</sup> However, the change in our synthesis conditions led to obtain a large solid product with different morphological shape and properties (see Figures S1 and S2, Supporting Information).

The morphology of as-synthesized samples characterized by FE-SEM (Figure 1 (A)) reveals that the nanorods have an average diameter of 200 nm and a length of up to several micrometers. A nanorod looks like a single crystal, and no pore is observed along its length. The elemental analysis of as-synthesized nanorods using SEM-EDS (Figure 1(B)) indicates the presence of C, O, Co, Cl, and Pt. The existence of Pt and Cl

peaks was due to the coating layer of sample and the unreacted CoCl<sub>2</sub>, respectively. In turn, the presence of C, O, and Co was due to the formation of cobalt basic carbonate phase. These results indicated the formation of intermediate Co<sup>II</sup>(OH)<sub>x</sub>(CO<sub>3</sub>)<sub>b</sub>Cl<sub>(2a+b)</sub>nH<sub>2</sub>O phase, as recently reported by Wang et al.<sup>14</sup> Moreover, the XRD pattern of hydrothermal product (see Figure S4, Supporting Information) exhibits typical diffraction peaks of orthorhombic cobalt basic carbonate Co(OH)<sub>x</sub>(CO<sub>3</sub>)<sub>0.5</sub>·0.11H<sub>2</sub>O phase (JCPDS, 48-0083).

The porous Co<sub>3</sub>O<sub>4</sub> nanorods were obtained after calcination of the as-synthesized products at 500 °C for 8 h, as shown in Figure 1(C). The diameter and length of porous Co<sub>3</sub>O<sub>4</sub> nanorods are similar to those of as-synthesized nanorods. Interestingly, the porous nanorods were formed from interconnected nanoparticles with average particles size of 100 nm. Air voids or pores are also clearly observed along the nanorods. No surfactant or structure-directing agent was used, but the porous-structured Co<sub>3</sub>O<sub>4</sub> was still obtained. The porous structure of the nanorods was formed during oxidation process. In such a process, the Co(OH)<sub>x</sub>(CO<sub>3</sub>)<sub>0.5</sub>·0.11H<sub>2</sub>O was oxidized to from Co<sub>3</sub>O<sub>4</sub> according to the following reaction



The Co<sub>3</sub>O<sub>4</sub> nanocrystals having different orientations grew up and attached together to form porous nanorods during oxidation.<sup>16</sup> The SEM-EDS spectrum of calcined nanorods (Figure 1(D)) reveals the presence of C, O, Pt, and Co elements. The O and Co were originally found in the Co<sub>3</sub>O<sub>4</sub> nanorods, which had a [Co]/[O] ratio of 0.70. This value is lower than that of stoichiometric Co<sub>3</sub>O<sub>4</sub> (0.75) because of the accession of oxygen. The crystal structure of the calcined Co<sub>3</sub>O<sub>4</sub> powders was characterized using XRD and is shown in Figure 1(E). The XRD pattern was indexed at the typical diffraction peaks of cubic Co<sub>3</sub>O<sub>4</sub> (JCPDS, 42-1467). There was no peak of other

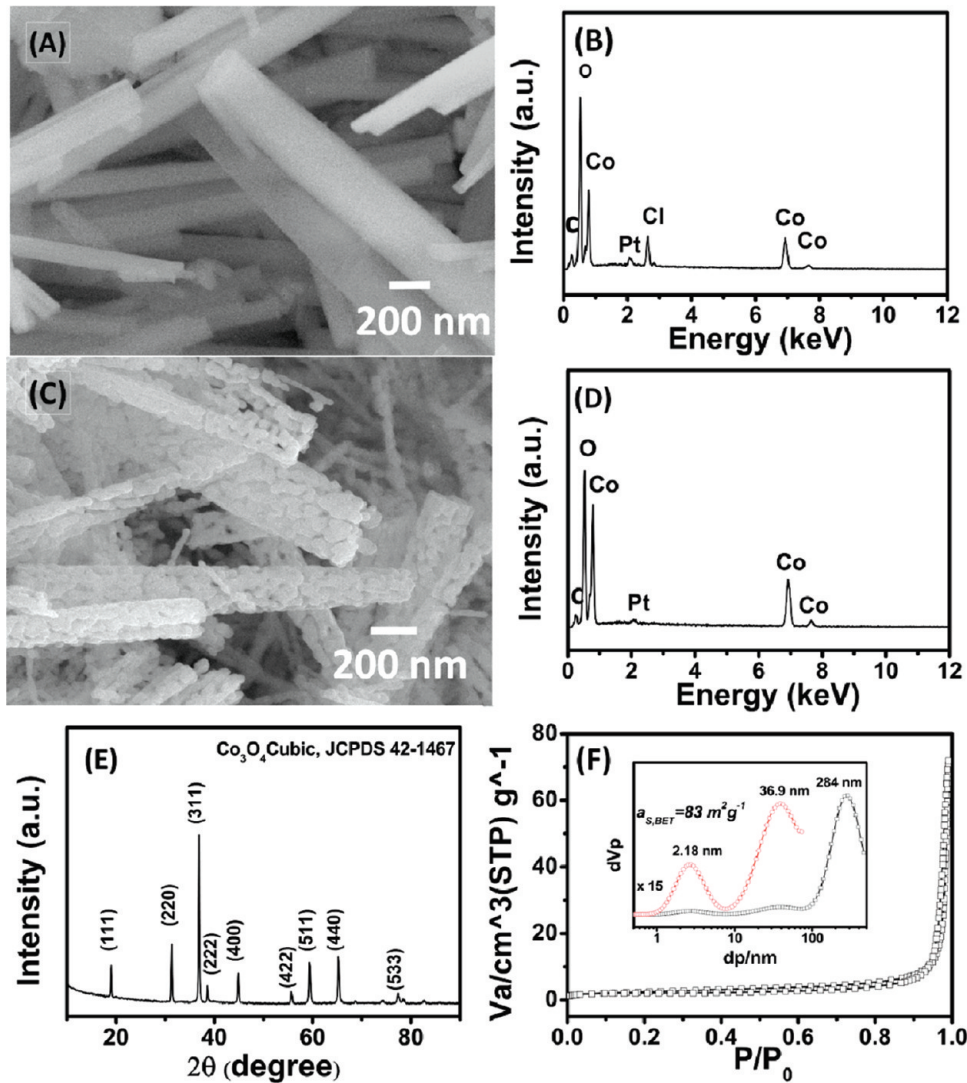


**Figure 1.** (A) SEM image and (B) EDS of as-synthesized nanorods, (C) FE-SEM image, (D) EDS, (E) XRD pattern, and (F)  $\text{N}_2$  isotherms adsorption of calcined porous  $\text{Co}_3\text{O}_4$  nanorods.

impurities observed, indicating the formation of single-phase  $\text{Co}_3\text{O}_4$ . The  $\text{N}_2$  isotherm adsorption/desorption of porous  $\text{Co}_3\text{O}_4$  nanorods measured at 77 K is shown in Figure 1(F). The specific surface area of the nanorods calculated from the  $\text{N}_2$  isotherm adsorption/desorption is  $83 \text{ m}^2 \text{ g}^{-1}$ . The pore size distribution (Figure 1(F)-, inset) shows the meso- and macro-porous structures with pore sizes of 2.18, 36.9, and 284 nm. The porous structure of the nanorods is good for application to gas sensors because the tunable pores of the nanorods allow the gas molecules to easily penetrate and adsorb on the surface of the nanorods, leading to fast response and recovery time as well as high sensitivity.

The HRTEM images and ED pattern of the as-synthesized  $\text{Co(OH)}_x(\text{CO}_3)_{0.5}\cdot0.11\text{H}_2\text{O}$  nanorods are shown in parts (A)-(C) and (A)-inset, respectively, of Figure 2. Figure 2(A) reveals that the as-synthesized nanorods have an average diameter of  $\sim 200 \text{ nm}$  and a length of up to  $4 \mu\text{m}$ . The nanorods are smooth and condensed without any pore along the rods. The HRTEM image, which is focused on the tip of a nanorod (Figure 2(B)), demonstrates the high crystallinity of as-synthesized nanorods. No crystalline boundary is observed

in the HRTEM image indicating that the nanorod is a single crystal. This result is consistent with the ED pattern (Figure 2(B), inset) that shows the bright dot arrays. The HRTEM image of as-synthesized nanorods did not show any grain boundary, whereas the ED pattern showed highly orientational bright dots (spots), agreed well with the orthorhombic  $\text{Co}(\text{OH})_x(\text{CO}_3)_{0.5}\cdot0.11\text{H}_2\text{O}$  crystal phase. Higher magnification of HRTEM (Figure 2(C)) shows clear lattice space of 0.24 nm, corresponding to the interplanar space of (301) planes of  $\text{Co}(\text{OH})_x(\text{CO}_3)_{0.5}\cdot0.11\text{H}_2\text{O}$ .

Figure 2 (D)-(I) shows the HRTEM images and ED pattern of  $\text{Co}_3\text{O}_4$  nanorods after calcination at  $500^\circ\text{C}$  for 8 h. As revealed in Figure 2(D), the nanorods became porous after calcination. Some air voids could be clearly observed along the nanorods. The average size of the calcined nanorods was consistent with that of the as-synthesized nanorods. HRTEM image of porous  $\text{Co}_3\text{O}_4$  nanorod (Figure 2(E)) demonstrated that the nanorod was formed from nanocrystals of about 70 nm in diameter and 100 nm in length. The ED pattern recorded on a single nanocrystal (Figure 2(E)-inset) showed the bright dots arrays, indicating that the particle, which formed the porous  $\text{Co}_3\text{O}_4$

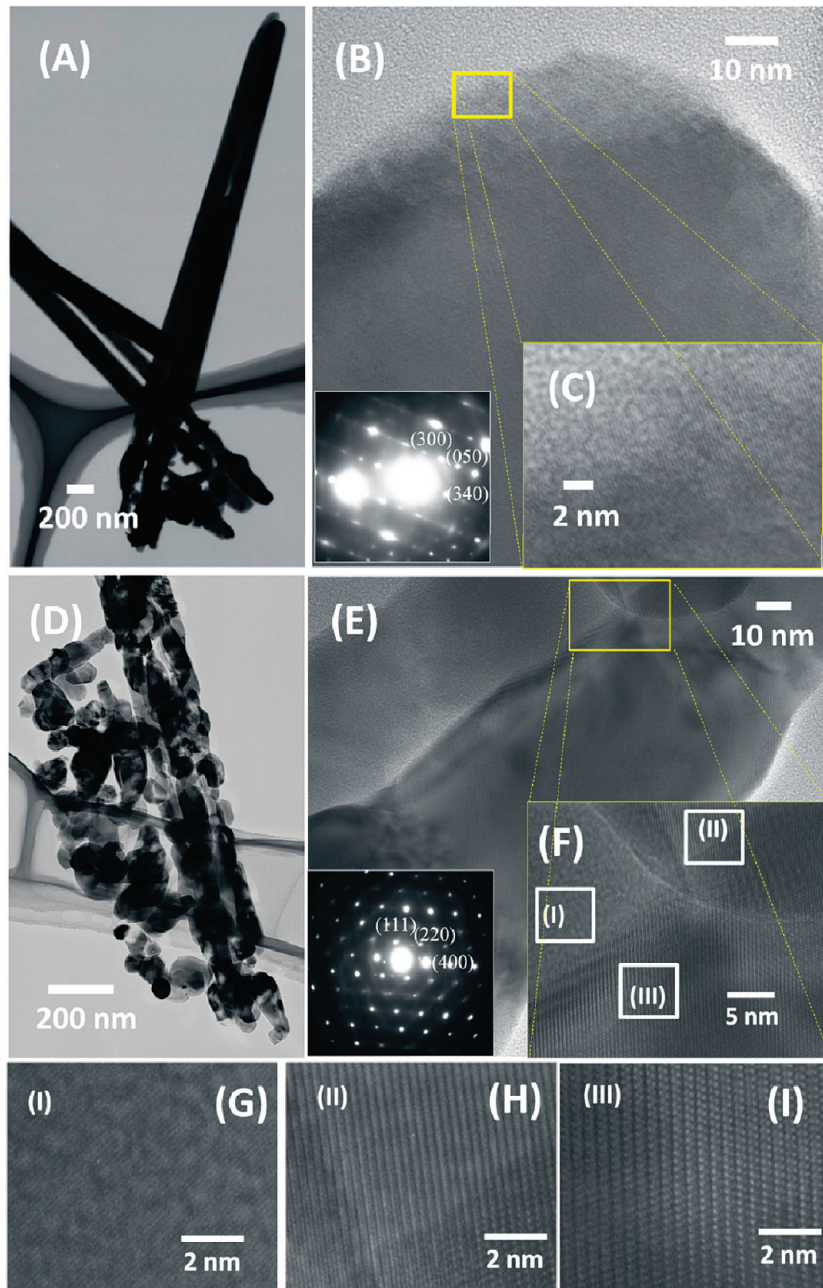


**Figure 2.** TEM and HRTEM images (insets are selective area electron diffraction (SAED)) of ((A)-(C)) as-synthesized  $\text{Co}(\text{OH})_x(\text{CO}_3)_{0.5}\cdot 0.11\text{H}_2\text{O}$ ; and ((D)-(I)) calcined  $\text{Co}_3\text{O}_4$  nanorods, respectively.

nanorods, was highly crystalline. The high crystallinity of porous  $\text{Co}_3\text{O}_4$  nanorods is very important in increasing the long-term stability of the sensors. A higher magnification of an HRTEM image focusing on the grain boundary between nanocrystals is shown in Figure 2(F). The enlarged HRTEM images of selected areas, marked as (I), (II), and (III) in Figure 2(F), are shown in Figure 2(G)-(I), respectively. These results indicate that the nanorods are highly crystalline and that each nanocrystal has a different orientation. The lattice spaces are 0.14 nm for area (I), 0.28 nm for area (II), and 0.46 nm for area (III), which correspond to the distances between (440), (220), and (111) planes of cubic  $\text{Co}_3\text{O}_4$  (JCPDS, 42-1467), respectively.

The morphology and the EDS mapping of meso- and macro-porous  $\text{Co}_3\text{O}_4$  nanorods were further characterized using STEM

and STEM-EDS, as shown in Figure 3 (A)-(D). A STEM image (Figure 3(A)) confirms the formation of porous  $\text{Co}_3\text{O}_4$  nanorods. The nanorods have an average diameter of 200 nm, a value confirmed by the FE-SEM and the HRTEM results. The STEM-EDS mapping of  $\text{Co}_3\text{O}_4$  nanorods exhibits the presence of O, Co, and C (Figure 3(B)-(D)). However, the contribution of O and Co is mainly from nanorods (Figure 3(C)), whereas that of C is originally from the TEM grid (Figure 3(D)). The STEM-EDS mapping also indicates that Co and O atoms are uniformly distributed in the nanorods. There was no significant difference in the atomic distribution of Co and O in the center of crystal and at the boundaries between nanocrystals.

**3.2. Characteristics of Gas Sensors. Gas-Sensing Assays.** The I(A)-V(V) plots of sensors measured in the presence of

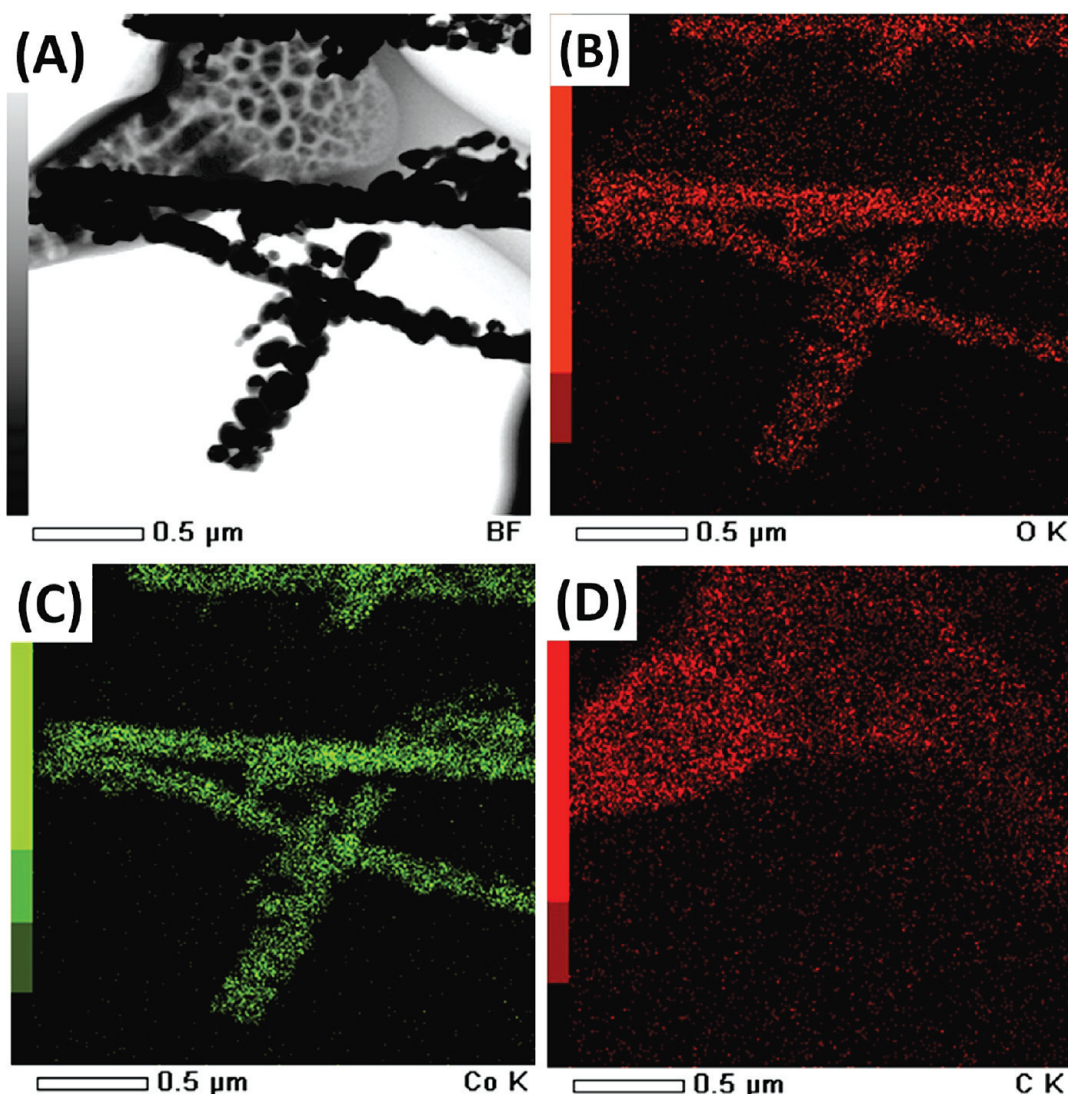


**Figure 3.** STEM image and STEM-EDS mapping of porous  $\text{Co}_3\text{O}_4$  nanorods: (A)-STEM image, (B)-oxygen, (C)-cobalt, and (D)-carbon mapping.

$\text{N}_2$  at different temperatures are shown in Figure 4(a). The plots reveal a linear dependence of current on applied voltage, which indicate that Ohmic contact was formed between the nanorods and the electrodes. The Ohmic contact is very important for characterizing the electrical properties of nanorods because this ensures that all upcoming sensing behaviors of sensors represent the properties of the nanorods but not the contact between the nanorods and the electrodes. The electrical current of the sensors increased with an increase in temperature, ranging from 200 to 300 °C, because of the semiconducting properties of the nanorods. However, with further increases in temperature, from 300 to 350 °C, the electrical current decreased. This behavior is possibly due to the adsorption/interaction of  $\text{N}_2$  to/with the  $\text{Co}_3\text{O}_4$  nanorods at high temperature.

The ethanol-sensing properties of the sensors measured at 300 and 350 °C, using  $\text{N}_2$  as carrier (and reference) gas, are shown in Figure 4(b). At both measured temperatures, the sensor resistance decreased upon exposure to ethanol and recovered approximately to the initial value when the chamber was refreshed with  $\text{N}_2$ . The sensor response to 20552 ppm ethanol calculated at the first cycle was 681 and 193% for the operating

temperatures of 350 and 300 °C, respectively. However, sensor response decreased gradually to 262 and 158% (at 350 °C) and 53 and 30% (at 300 °C) in the second and third cycles, respectively. This finding demonstrates that  $\text{N}_2$  is not a suitable carrier and reference gas for gas-sensing measurement. There was a decrease in sensor resistance upon exposure to ethanol (a similar behavior was also found for acetone but data are not shown here). This behavior is very interesting in understanding the sensing mechanism of the sensors. Normally, the resistance of a p-type semiconductor ( $\text{Co}_3\text{O}_4$ ) is expected to increase upon exposure to reducing gas (ethanol).<sup>13</sup> Upon exposure, the ethanol molecules interact with preadsorbed oxygen on the surface of  $\text{Co}_3\text{O}_4$  and release free electrons to the nanorods. The released electrons neutralize the hole carriers in the  $\text{Co}_3\text{O}_4$  p-type semiconductor and increase the sensor resistance. However, in this study, the sensing properties were measured with  $\text{N}_2$  as carrier and reference. In using  $\text{N}_2$  as carrier gas, there was a lack of preadsorbed oxygen on the surface of the  $\text{Co}_3\text{O}_4$ . Therefore, the ethanol molecules interacted directly with the  $\text{Co}_3\text{O}_4$  crystals. The direct adsorption of ethanol on the surface of  $\text{Co}_3\text{O}_4$  possibly led to a decrease in sensor resistance.

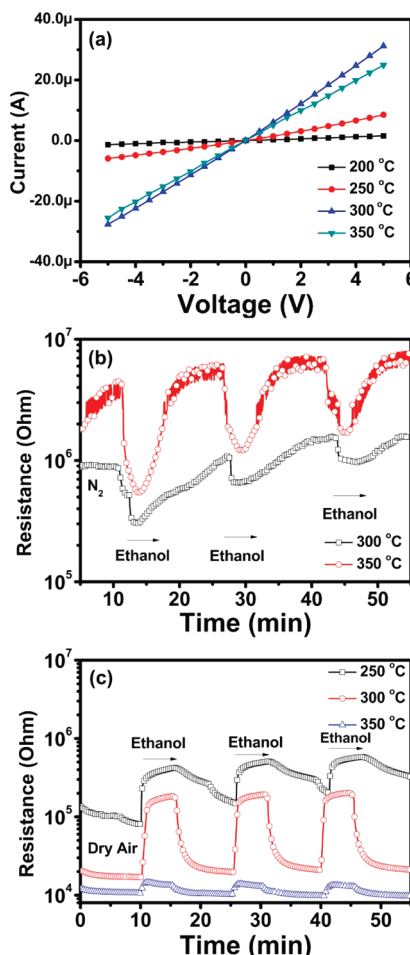


**Figure 4.** Electrical and gas sensing properties of meso-macroporous  $\text{Co}_3\text{O}_4$  nanorods based gas sensor: (a) I(A)-V(V) plots; (b) ethanol sensing measured at different temperature using  $\text{N}_2$  as reference; and (c) ethanol sensing measured at different temperature using dry air as reference.

To confirm this, the ethanol-sensing properties of  $\text{Co}_3\text{O}_4$  were again measured at different temperatures but with dry air as carrier and reference gas. The change in sensor resistance after a three cycle' exposure to ethanol is shown in Figure 4(c). As expected, the sensor resistance increased abruptly in the presence of ethanol and decreased to its initial value when the chamber was refreshed with dry air. Additionally, the sensor showed a very stable signal after three cycles, switching on/off between dry air and ethanol, and then back to dry air. These results confirm that the abnormal property found in Figure 4(b) is due to the effect of the  $\text{N}_2$  environment. Moreover, we discovered that the initial resistance measured in dry air was lower than the value measured in  $\text{N}_2$ . The sensor response to 20552 ppm of ethanol calculated from Figure 4(c) is 307, 1036, and 38% for operating temperatures of 250, 300, and 350 °C, respectively. These results indicate that the sensor measured in dry air had a lower optimal working temperature (300 °C compared with 350 °C) and has a higher the maximum value of response (1036% compared with 681%).

Figure 5(a) presents the change in sensor resistance upon exposure to different concentrations of acetone, ethanol, and benzene. Each concentration was exposed for two or three cycles to study its stability, response, and recovery. The sensor showed

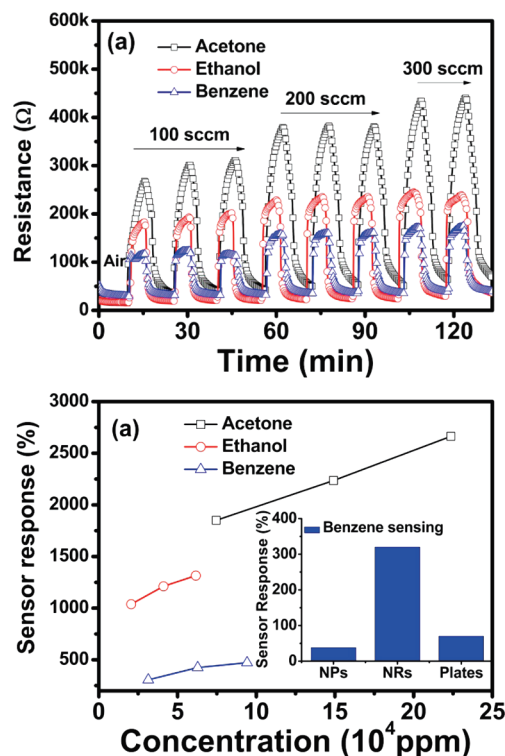


**Figure 5.** Gas sensing properties of porous  $\text{Co}_3\text{O}_4$  nanorods to acetone, ethanol, and benzene measured at 300 °C: (a) the change in sensor resistance upon exposure to different concentration of acetone, ethanol, and benzene and (b) sensor response as a function of gases concentration; ((b)-inset) the response to benzene of nanoparticles (NPs), meso-/macroporous nanorods (NRs) and porous plates (plates).

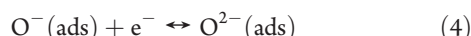
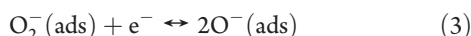
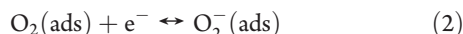
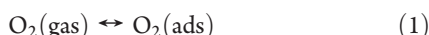
very stable signal and good response and recovery after several cycles of switching on/off between dry air and tested gas and then back to dry air. The calculated response time [ $t_{90\%(\text{air-to-gas})}$ ] and recovery time [ $t_{90\%(\text{gas-to-air})}$ ] were 0.26 and 2 min for benzene, 0.31 and 2.5 min for ethanol, and 0.4 and 3 min for acetone, respectively. The fast response time of less than a minute is effective in the rapid detection of flammable and toxic gases. The fast response time may have been due to the tunable porous structure of the nanorods, which enhanced the diffusion and the adsorption rate of gas molecules on the surface of the  $\text{Co}_3\text{O}_4$ .

Figure 5(b) shows sensor response as a function of gases concentration. Sensor response is highest for acetone, followed by ethanol and benzene. The sensor response was 1850%, 2236%, and 2664% for 74570, 149111, and 223666 ppm concentration of acetone, respectively. The linear dependence of sensor response as a function of acetone concentration in measured range is one of the advances in its practical application because of the easy design in the read-out signal circuit. Moreover, the sensor can detect concentrations of acetone of up to 223666 ppm without significant saturation. This ensures that the sensor can be used to detect the acetone in the explodable and/or flash fireable concentrations.

To demonstrate the sensing efficiency of meso-/macroporous  $\text{Co}_3\text{O}_4$  nanorods among the various gas sensors, the sensitivity of meso-/macroporous  $\text{Co}_3\text{O}_4$  nanorods was compared to that of nanoparticles and porous plates as shown in Figure 5(b)-inset. The response of meso-/macroporous nanorods is 7.1 folds and 4 folds higher than that of nanoparticles and porous plates,

respectively. This finding indicates that the meso-/macroporous nanorods have the potential for gas sensor application. In turn, the meso-/macroporous  $\text{Co}_3\text{O}_4$  nanorods showed relatively low sensitivity to acetone (1850% for 74570 ppm) compared with the  $\text{Co}_3\text{O}_4$  hollow nanosphere sensors (650% to 1000 ppm).<sup>17</sup> However, the sensor based on  $\text{Co}_3\text{O}_4$  hollow nanospheres revealed a saturated response to gas concentration ranging from 200 to 1000 ppm. As a consequence, the meso-/macroporous  $\text{Co}_3\text{O}_4$  nanorod sensor designed in this study exhibited interesting sensing response behavior that permits the applicability of this sensor in potential devices. Despite the fact that the meso-/macroporous  $\text{Co}_3\text{O}_4$  nanorods-based sensor shows good response to acetone, ethanol, and benzene, it still requires further investigation of the long-term stability of this gas device for real application as a sensor.

**Gas-Sensing Mechanism.** Based on the finding on the effects of carrier gas on the sensing properties of meso-/macroporous  $\text{Co}_3\text{O}_4$  nanorods, the gas-sensing mechanism of the device can be described as follows. When measuring, with dry air as carrier and reference gas, the oxygen molecules in the air are adsorbed on the surface of the  $\text{Co}_3\text{O}_4$  (according to eqs 1 to 4 below) and capture electrons from the  $\text{Co}_3\text{O}_4$ . Inasmuch as  $\text{Co}_3\text{O}_4$  is a p-type semiconductor with hole carriers,<sup>6</sup> the adsorption of the oxygen molecules results in an increase in the carrier density on the surface of the nanorods and the formation of a conduction layer on the surface of the  $\text{Co}_3\text{O}_4$



The adsorbed oxygen is mainly in the form of  $\text{O}^-$ , at temperatures ranging from 200 to 350 °C.<sup>9</sup> Therefore, when exposed to ethanol, the  $\text{C}_2\text{H}_5\text{OH}$  molecules interact with preadsorbed oxygen as depicted in eq 5. The interaction between ethanol and preadsorbed oxygen releases free electrons. Those released electrons neutralize the holes in the  $\text{Co}_3\text{O}_4$  (eq 6), which results in a decrease in the number of hole carriers in  $\text{Co}_3\text{O}_4$ , and, consequently, an increase in sensor resistance



During sensing measurement, the oxygen molecules are continuously supplied from the dry air (carrier gas) and adsorbed on the  $\text{Co}_3\text{O}_4$  surface, whereas the interaction with ethanol continuously caused water and carbon dioxide molecules to escape from the surface. The sensor resistance increased until a dynamic equilibrium condition was obtained. When the flow of ethanol stopped, oxygen molecules (in the air) were adsorbed on the surface of the  $\text{Co}_3\text{O}_4$  (eqs 1-4), and sensor resistance decreased to their initial values. Similar reactions happened when ethanol was replaced with acetone or benzene. A different behavior was observed when the sensor was measured in  $\text{N}_2$ . Due to the lack of preadsorbed oxygen, the test gas molecules directly absorbed on the surfaces of  $\text{Co}_3\text{O}_4$  nanorods. Thus, the gas molecules partially reduced the  $\text{Co}_3\text{O}_4$  to Co and led to decrease the sensor resistance.<sup>18</sup> The slow recovery and the drift of sensor resistance

after stopping the flow of the test gas were caused by the release of oxygen in the crystal and the reoxidation.

## 4. CONCLUSION

Large yields of crystalline meso- and macroporous  $\text{Co}_3\text{O}_4$  nanorods have been successfully synthesized using the hydrothermal method and without using any surfactants or structure-directing agents for gas sensor applications. The fabrication fulfills the growing demand for a simple, low-cost, mass-produced, and controllable synthesis of meso- and macroporous  $\text{Co}_3\text{O}_4$  nanorods for thick-film gas sensors technology. The synthesized nanorods were found to be effective in the detection of acetone, benzene, and ethanol. It has good stability, high sensitivity, and fast response and recovery time. The sensitivity of meso- and macroporous nanorods is 7.1 folds and 4 folds higher than that of nanoparticles and porous plates, respectively. In addition, the effect of carrier gases on the sensing properties of  $\text{Co}_3\text{O}_4$  was investigated to clarify the sensing mechanism of nanorods, where the preadsorbed oxygen decided the sensing of  $\text{Co}_3\text{O}_4$ . This finding is a key factor in understanding the gas-sensing mechanism of  $\text{Co}_3\text{O}_4$ -based gas sensors.

## ■ ASSOCIATED CONTENT

**S Supporting Information.** The yield of hydrothermal products of nanocrystals, FESEM image of porous  $\text{Co}_3\text{O}_4$  nanorods, cross sectional FESEM image of sensor, and XRD pattern of as-synthesized nanorods (hydrothermal product). This material is available free of charge via the Internet at <http://pubs.acs.org>.

## ■ AUTHOR INFORMATION

### Corresponding Author

\*E-mail: sherif.elsafty@nims.go.jp.

## ■ ACKNOWLEDGMENT

We express our thanks to the Japan Society for Promotion Science (JSPS) for financial support (Grant No. P09606).

## ■ REFERENCES

- (a) Bytnarowicz, A.; Badea, O.; Popescu, F.; Musselman, R.; Tanase, M.; Barbu, I.; Frączek, W.; Gembas, N.; Surdu, A.; Danescu, F.; Postelnicu, D.; Cenusă, R.; Vasile, C. *Environ. Pollut.* **2005**, *137*, 546–567. (b) Cox, R. M. *Environ. Pollut.* **2003**, *126*, 301–311. (c) El-Safty, S. A.; Ismail, A. A.; Matsunaga, H.; Nanjo, H.; Mizukami, F. *J. Phys. Chem. C* **2008**, *112*, 4825–4835.
- (2) Hubálek, J.; Malysz, K.; Práek, J.; Vilanova, X.; Ivanov, P.; Llobet, E.; Brezmes, J.; Correig, X.; Sverák, Z. *Sens. Actuators, B* **2004**, *101*, 277–283.
- (3) (a) Pearton, S. J.; Ren, F.; Wang, Y. L.; Chu, B. H.; Chen, K. H.; Chang, C. Y.; Lim, W.; Lin, J.; Norton, D. P. *Prog. Mater. Sci.* **2010**, *55*, 1–59. (b) Eranna, G.; Joshi, B. C.; Runthala, D. P.; Gupta, R. P. *Crit. Rev. Solid State Mater. Sci.* **2004**, *29*, 111–188.
- (4) (a) Xu, H.; Liu, X.; Cui, D.; Li, M.; Jiang, M. *Sens. Actuators, B* **2006**, *114*, 301–307. (b) Thong, L. V.; Hoa, N. D.; Le, D. T. T.; Viet, D. T.; Tam, P. D.; Le, A. T.; Hieu, N. V. *Sens. Actuators, B* **2010**, *146*, 361–367.
- (5) (a) Patil, L. A.; Shinde, M. D.; Bari, A. R.; Deo, V. V. *Sens. Actuators, B* **2009**, *143*, 270–277. (b) Jiang, L. Y.; Wu, X. L.; Guo, Y. G.; Wan, L. J. *J. Phys. Chem. C* **2009**, *113*, 14213–14219. (c) Zuruzi, A. S.; MacDonald, N. C.; Moskovits, M.; Kolmakov, A. *Angew. Chem., Int. Ed.*

- 2007, 46, 4298–4301. (d) Zhang, D.; Liu, Z.; Li, C.; Tang, T.; Liu, X.; Han, S.; Lei, B.; Zhou, C. *Nano Lett.* **2004**, 4, 1919–1924.
- (6) (a) Zhang, J.; Liu, J.; Peng, Q.; Wang, X.; Li, Y. *Chem. Mater.* **2006**, 18 (4), 867–871. (b) Gou, L.; Wang, G. X.; Yang, J.; Park, J. S.; Wexler, D. *J. Mater. Chem.* **2008**, 18, 965–969.
- (7) (a) Yamamoto, H.; Tanaka, S.; Naito, T.; Hirao, K. *Appl. Phys. Lett.* **2002**, 81, 999–1001. (b) Mousavand, T.; Naka, T.; Sato, K.; Ohara, S.; Umetsu, M.; Takami, S.; Nakane, T.; Matsushita, A.; Adschariri, T. *Phys. Rev. B* **2009**, 79, 144411. (c) Tiana, Z.; Bahlawane, N.; Qia, F.; Kohse-Höinghaus, K. *Catal. Commun.* **2009**, 11, 118–122. (d) Jiang, J.; Liu, J. P.; Huang, X. T.; Li, Y. Y.; Ding, R. M.; Ji, X. X.; Hu, Y. Y.; Chi, Q. B.; Zhu, Z. H. *Cryst. Growth Des.* **2010**, 10, 70–75.
- (8) Zhang, M.; Jiang, G. *Chin. J. Chem. Phys.* **2007**, 20, 315.
- (9) Patil, D.; Patil, P.; Subramanian, V.; Joy, P. A.; Potdar, H. S. *Talanta* **2010**, 81, 37–43.
- (10) Liao, L.; Lu, H. B.; Li, J. C.; He, H.; Wang, D. F.; Fu, D. J.; Liu, C.; Zhang, W. F. *J. Phys. Chem. C* **2007**, 111, 1900–1903.
- (11) (a) Masuda, Y.; Kato, K. *Cryst. Growth Des.* **2008**, 8, 2633–2637. (b) Tiemann, M. *Chem.-Eur. J.* **2007**, 13, 8376–8388.
- (12) (a) Tripathy, S. K.; Christy, M.; Park, N. H.; Suh, E. K.; Anand, S.; Yu, Y. T. *Mater. Lett.* **2008**, 62, 1006–1009. (b) Hu, L.; Peng, Q.; Li, Y. *J. Am. Chem. Soc.* **2008**, 130, 16136–16137. (c) Zhang, H.; Wu, J.; Zhai, C.; Ma, X.; Du, N.; Tu, J.; Yang, D. *Nanotechnology* **2008**, 19, 035711 (Spp).
- (13) He, T.; Chen, D.; Jiao, X.; Wang, Y.; Duan, Y. *Chem. Mater.* **2005**, 17 (15), 4023–4030.
- (14) Wang, G.; Shen, X.; Horvat, J.; Wang, B.; Lin, H.; Wexler, D.; Yao, J. *J. Phys. Chem. C* **2009**, 113, 4357–4361.
- (15) Hoa, N. D.; Quy, N. V.; Kim, D. J. *Sens. Actuators, B* **2009**, 142, 253–259.
- (16) Penn, R. L.; Banfield, J. F. *Science* **1998**, 281, 969–971.
- (17) Park, J.; Shen, X.; Wang, G. *Sens. Actuators, B* **2009**, 136, 494–498.
- (18) Llorca, J.; Piscina, P. R.; Dalmon, J. A.; Homs, N. *Chem. Mater.* **2004**, 16, 3573–3578.